High Circular Dichroism Chiral Sensor Based on the Combination of Nanorods and Annular Cylinders

Peipei Wang, Ziang Gao, Yang He, Zhengshan Xu, and Tonggang Zhao

Abstract—Chiral materials are crucial components in the natural world, and the exploration of chiral materials hold significant importance in advancing areas such as chiral sensing, bio-marking. The integration of Bound States in the Continuum (BICs) in the design of chiral metasurfaces has emerged as a focal point in optical research, offering widespread research value and practical applications. The chiral dielectric metasurface proposed in this paper is formed by a combination of silicon nanorod, annular cylinder, and silicon dioxide substrate. Through selective detaching, we simultaneously break the structural mirror symmetry and in-plane inversion symmetry, thereby eliciting quasi-BICs and intrinsic chirality. This design achieves dual-band chiral responses, yielding a maximum circular dichroism (CD) of 0.979 and a Q-factor of 1517.5. By adjusting the structural parameters, the tunability of the structure is achieved. The study of the sensing performance of the metasurface resulted in a maximum sensitivity (S) of 270.6 nm/RIU and a maximum Figure of Merit (FOM) of 587.5. Additionally, By comparing the sensing performance with achiral structure, we verified the enhancement of sensing performance through chiral effects. The proposed chiral metasurface advances the practical application of chirality in fields such as biosensing.

Index Terms—All-dielectric metasurfaces, maximum chirality, circular dichroism (CD), refractive index sensor.

I. Introduction

METASURFACES are two-dimensional planar structures composed of artificial atoms with special electromagnetic properties arranged in a certain pattern. It enables flexible control of the amplitude, phase, polarization, and other characteristics of incident light, showing powerful capabilities in the optical field manipulation. Metasurfaces possess unique advantages in wavefront control and localized field enhancement, demonstrating distinctive strengths in [1], [2], [3]. Through the design of artificial structural units and their arrangement, metasurface can exhibit optical response characteristics not found in natural materials, garnering widespread attention and gradually becoming a hot research topic. They are anticipated to become an indispensable component in future optical systems. In comparison to metamaterials, metasurfaces not only break through the limitations of traditional material electromagnetic properties but also overcome the challenges associated with the three-dimensional structure of metamaterials. The two-dimensional planar structure of metasurfaces facilitates the integration and miniaturization of nanophotonic devices, providing convenience for advanced applications in optics and having been widely used in various fields [4]. H.Yang et al. had successfully fabricated a bi-band chromatically corrected metasurface lens achieving substantial focusing efficiencies of 54% and 70% respectively [5]. S. Wang et al proposed and demonstrated a solid Pancharatnam-Berry (PB) sphere polarizer based on metasurfaces, which can convert unpolarized incident beams into polarization at any point inside the solid PB sphere [6].

Chirality refers to the property of objects in the natural world that cannot be overlapped with their mirror images through rotation and moving, much like the inability to superimpose one's left and right hands. Chirality is widespread in nature, with important biological components such as proteins, Deoxyribo Nucleic Acid(DNA), amino acids, nucleic acids, exhibiting chirality. Chiral substances respond differently to asymmetric electromagnetic fields, a phenomenon known as chiroptical effects, including Circular Dichroism (CD) and Optical Rotation (OR). Research on chiral materials is crucial for advancing developments in biolabeling, chiral analysis and detection, sensing, and optoelectronic applications. However, naturally occurring chiral materials exhibit very weak optical responses, often confined to the near-ultraviolet range, significantly limiting their detection sensitivity and applications [7], [8]. Chiral metasurfaces generate chiral signals that are orders of magnitude stronger than those from natural chiral materials. These signals can extend into the visible and near-infrared spectrum. Moreover, the geometric shapes of chiral metasurfaces can be arbitrarily controlled, and their optical responses can be tailored by adjusting the structural parameters of the chiral metamaterial. This presents a wide range of applications in various fields, indicating promising prospects for the development of chiral metasurfaces [9], [10]. In 2023, Hwaseob Lee demonstrated that a Mie-resonant metamaterial resonator, composed of a symmetrical and asymmetrical Mie scatterer pair, could reach exceptional points or chosen chirality while efficiently suppressing backscattering [11].

In order to further enhance the interaction between light and matter, the combination of chiral metasurfaces with Bound States in the Continuum (BICs) has become a research hotspot. BICs are localized states that coexist with extended modes

within the light cone, characterized by zero linewidth and an infinite Q-factor as they do not couple to free-space radiation. This unique property has garnered significant attention [12], [13], [14], [15]. True BICs exist only in ideal lossless structures and can achieve perfect energy confinement. BICs modes can be transformed into quasi-BICs modes by breaking symmetry. Unlike BICs modes, the Q-factor of quasi-BICs can be adjusted by the degree of asymmetry. When the asymmetry is very small, quasi-BICs modes exhibit extremely high Q-factor. The transition process from BICs states to quasi-BICS states can be verified by calculating the Q-factor and the square inverse law they satisfy [16], [17], [18], [19], [20]. Recent research has shown that optical metasurfaces with high Q-factor chiral resonances can induce strong interactions between chiral optical fields and chiral materials. Combining BICs with chiral metasurfaces can achieve both high Q-factor and strong CD, which is crucial for advancing applications in chiral optics [21], [22], [23], [24]. In 2020, Adam O. and colleagues combined Fano resonance with chiral metasurfaces, designing chiral metasurfaces with sharp Fano resonance spectra [25]. Maxim V. G. proposed a chiral BICs metasurface based on dielectric rod pairs in 2020 and numerically verified the maximum chirality of quasi-BICs resonances [26]. In 2022, Tan S. et al utilized symmetry-reduced high birefringence quasi-atoms to support elliptical eigenstates with opposite helicity, providing a convenient method to achieve maximum planar chirality by breaking in-plane structural symmetry or changing the illumination angle [27]. Simultaneously, the strong CD of chiral materials holds great promise in various fields such as biology and chemistry for detection and sensing applications. Optical biosensing technology involves using biochemical substances as the detection samples, such as proteins and nucleic acids. By detecting various spectral changes caused by these biochemical molecules, optical biosensing technology is of significant value for the real-time clinical assessment of diseases [28], [29], [30]. Currently, the predominant trend in chiral sensing is the utilization of chiral bio-substances for sensing. However, this metasurface sensing platform is limited to detecting only chiral substances. In contrast, spectral sensing, which relies on refractive index detection, offers a broader spectrum of sensing capabilities. Beyond its application in chiral bio-sensing, it holds significant potential for environmental monitoring and other domains, underscoring its research value [31], [32]. In 2022, Jin P. and colleagues conducted a sensitivity analysis based on both chiral and non-chiral modes, achieving a refractive index sensitivity of up to 128.5 GHz/RIU (Refractive Index Unit) [33].

In this paper, we have designed a chiral all-dielectric metasurface based on the combination of nanorods and annular cylinders. The metasurface consists of a central silicon nanorod and symmetrically arranged silicon annular cylinders on both sides. By selectively detaching one of the annular cylinders to break the structural symmetry, we achieve a high Q-factor based on BICs and nearly unity CD. The maximum Q-factor and CD are found to be 1517.5 and 0.93, respectively. Furthermore, we investigate the sensing characteristics of this chiral structure by studying the CD spectral shift under different refractive index backgrounds. The sensitivity based on chiral CD reaches 270.6 nm/RIU, and the FOM value is as high as 587.5. This is of

importance for the application of chiral structures in sensing and detecting fields. Crucially, we have achieved multiple bands of CD spectral peaks and sensing characteristics, providing insights for subsequent research on ultra-broad detection and dynamic sensing of sensors.

II. STRUCTURE DESIGN

The designed metasurface is illustrated in Fig. 1. It consists of a silicon nanorod placed on a SiO_2 substrate and Si toroidal columns with opposite rotation directions initially placed symmetrically on both sides of the y axis. The unit cell parameters are set with a periodicity of $Px = Py = 800$ nm, thickness $t = 220$ nm, nanorod length in the middle $a = 400$ nm, width $b = 100$ nm, and inner and outer radii of the annular cylinders on both sides $r_1 = 170$ nm and $r_2 = 300$ nm, respectively. The background refractive index of the structure is 1.00, and the material data for Si and SiO_2 are referenced from Palik's optical handbook [34]. Asymmetry in the structure is introduced by detaching the left small annular cylinder. $\alpha = 120°$ represents the original central angle corresponding to the initial annular cylinder, and β denotes the central angle corresponding to the detached part of the left annular cylinder. In general, we can define the degree of asymmetry using geometric parameters. Here, we define the in-plane asymmetry parameter δ as the angle of the annular cylinder that has been detached, namely $\delta = \beta$.

Based on the finite difference time domain (FDTD) method, we conducted numerical analysis of the optical properties of the structure using the FDTD optical simulation module of Ansys Lumerical simulation and design software [35]. Under the original symmetrical structure, considering simulation time and convergence, the FDTD simulation settings include: anti-symmetric boundary conditions in the x-direction and symmetric boundary conditions in the y-direction, perfectly matched layer (PML) boundary conditions in the z-direction, and mess accuracy of 5. Under asymmetric structure, the x-axis and y-axis boundary conditions change to periodic boundary conditions.

While the study is confined to a simulation level, Fig. 2 not only validate the feasibility of the experiment but also illustrate the comprehensive process flow for fabricating such nanostructures. Initially, as depicted in Fig. 2(b), a Si film can be deposited on a SiO_2 substrate utilizing low-pressure physical vapor deposition (LPCVD). Subsequently, ZEP520A photoresist is spin-coated onto the silicon plane and then baked, as illustrated in Fig. 2(b). Electron beam lithography (EBL) and development techniques are then employed to yield nanohole arrays following inductively coupled plasma (ICP) etching [Fig. 2(d) and (e)]. The final step involves removing the photoresist and cleaning with deionized water [Fig. 2(f)]. The fabrication of desired metasurface requires only a few straightforward processes.

III. RESULTS AND DISCUSSION

The CD of the chiral structure is manifested as the difference in transmittance (or absorptance) between right circularly polarized (RCP) and left circularly polarized (LCP) waves and can
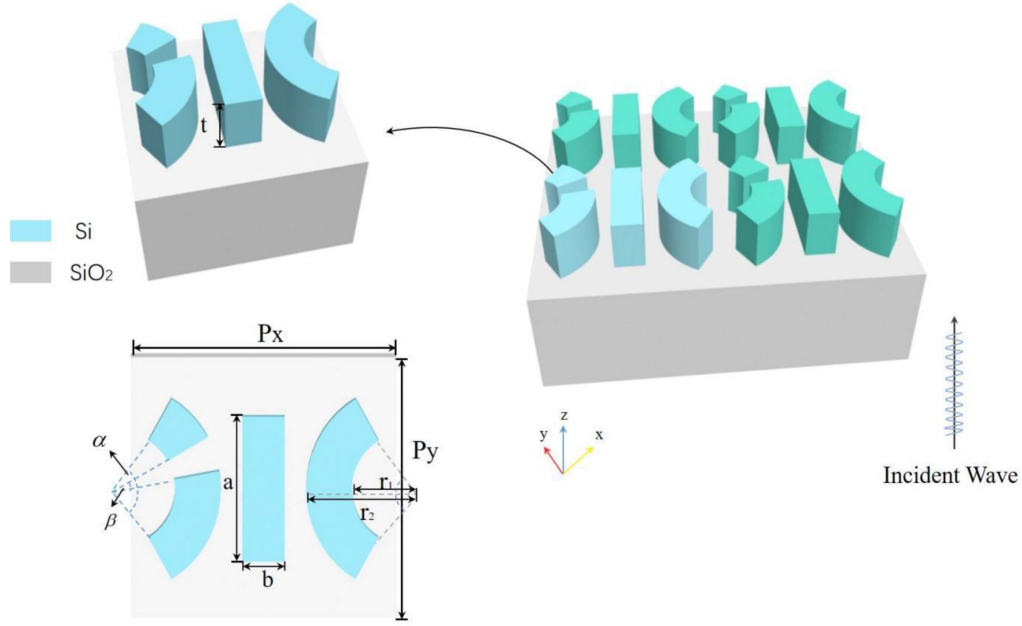
Fig. 1. Schematic diagram of the all-dielectric metasurface. The unit cell is composed of two initially symmetrically placed Si annular cylinders with opposite rotation directions and a centrally placed Si nanorod. Asymmetry in the structure is introduced by detaching the left annular cylinder. Px = Py = 800 nm, t = 220 nm, r_1 = 170 nm, r_2 = 300 nm, α = 120°. Other initial geometric parameters are as indicated in the figure.
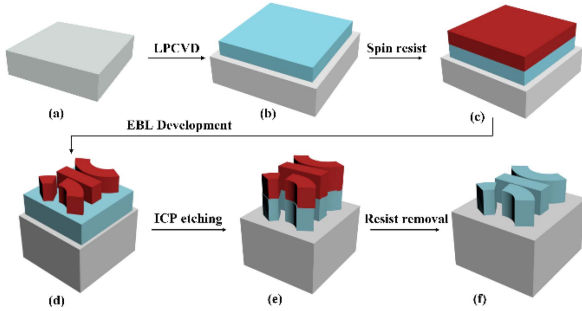

Fig. 2. The fabrication process diagram of the chiral metasurface.

be defined as follows:

$$CD = \frac{|(T_{rr} + T_{lr}) - (T_{rl} + T_{ll})|}{(T_{rr} + T_{lr}) + (T_{rl} + T_{ll})} \quad (1)$$

Where $T_{ij} = |t_{ij}|(i = r, l; j = r, l; i, j$ is RCP and LCP, respectively) is the transmittance from input polarization j to output polarization i. For example, T_{ll} and T_{rl} represent the transmittances of LCP and RCP after incidence, respectively. T_{ll} and T_{rr} are the co-polarized transmittance components for circularly polarized light, where T_{rl} and T_{lr} represent the cross-polarized transmittance components [36], [37]. All 'elements of matrix t_{ij} in the circular polarization basis constitute the *Jones matrix*:

$$J = \begin{pmatrix} t_{rr} & t_{rl} \\ t_{lr} & t_{ll} \end{pmatrix} \quad (2)$$

To investigate the chiral effects, circularly polarized light can be used as the incident source for the metasurfaces. Circularly

polarized light can be regarded as the superposition of two linearly polarized components with equal amplitudes, orthogonal polarization angles, and a phase change of 90 degree. In FDTD simulations, this can be implemented by adding two linearly polarized incidences at the same location with polarization angles change by 90 degrees in phase. When observed along the direction of light propagation, the clockwise rotation of the electric field vector corresponds to right-circularly polarized light, while counterclockwise rotation corresponds to left-circularly polarized light. Simultaneously, based on coordinate transformations, the relationship between the Jones matrix elements for circularly polarized light and linearly polarized light transmission are as follows:

$$J_{cirl} = \begin{pmatrix} t_{rr} & t_{rl} \\ t_{lr} & t_{ll} \end{pmatrix} = \wedge^{-1} J_{linear} \wedge$$

$$= \frac{1}{2} \begin{pmatrix} t_{xx} + t_{yy} + i(t_{xy} - t_{yx}) & t_{xx} - t_{yy} - i(t_{xy} + t_{yx}) \\ t_{xx} - t_{yy} + i(t_{xy} + t_{yx}) & t_{xx} + t_{yy} - i(t_{xy} - t_{yx}) \end{pmatrix} \quad (3)$$

Where $\wedge = \frac{1}{\sqrt{2}} \begin{pmatrix} 1 & 1 \\ i & -i \end{pmatrix}$ is the coordinate transformation matrix. Therefore, we can input only linearly polarized light and obtain circularly polarized transmittance components through coordinate transformation. This enables us to acquire the desired circular dichroism (CD) and investigate the chiral effects of the structure.

Fig. 3 displays the transmittance components and CD spectrum for the scenario where the left annular cylinder of the nanorod remains undetached, specifically when $\beta = 0$. Under the incidence of LCP and RCP in a structurally symmetric configuration, it is evident that the structure lacks chiroptical
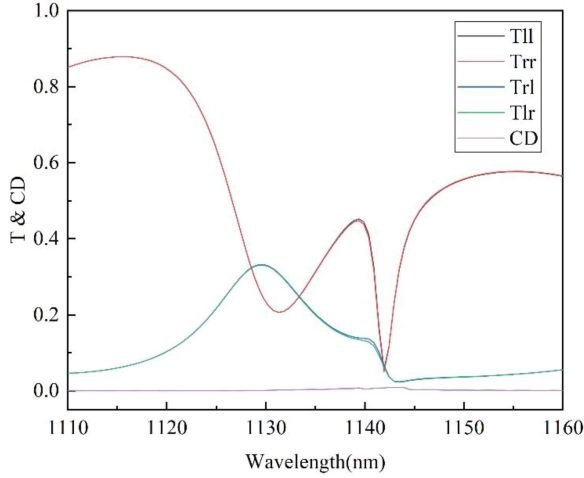
Fig. 3. Circularly polarized transmittance components and CD of the structure under structural symmetry.

effects (CD = 0). Furthermore, owing to reciprocity, $T_{ll} = T_{rr}$, $T_{rl} = T_{lr}$.

Achieving a high Q-factor with a compact structure is of paramount importance for a broad range of optical response characteristics and their applications, including chirality. BICs as a prominent strategy for attaining high-Q metasurfaces, has garnered extensive research attention. Symmetry-protected BICs, emerging from the disparity between the spatial symmetry of the mode and that of the external radiation waves, can be transformed into quasi-BICs mode with enhanced radiation channel and elevated Q-factor through symmetry-breaking methods, such as introducing asymmetry via oblique incidence or structural modification [38]. Additionally, investigations suggest that manipulating the localized response to birefringence through geometric structures possessing inversion symmetry allows for achieving impeccably in-plane chiral responses. Subsequently, breaking inversion symmetry through judicious perturbations induces intrinsic chirality based on quasi-BICs.

In this work, we selectively detached the left annular cylinder to simultaneously break the structural mirror symmetry and inversion symmetry. When $\delta = 30°$, the circularly polarized transmittance components and CD spectrum are depicted in Fig. 4(a) and (b), respectively:

In Fig. 4(a), it can be observed that at $\delta = 30°$, two mode peaks appear at 1130.4 nm (mode I) and 1140.4 nm (mode II). In mode I, the sum of Trr and Tlr are around 0.8, while Tll and Trl values are almost 0. This indicates that at 1130.4 nm, the structure predominantly transmits RCP light and almost entirely reflects LCP light, achieving nearly lossless maximal chirality. This is further supported by the CD spectrum in Fig. 4(b), where the CD peak at mode I reaches 0.93, demonstrating a strong chiral effect. At 1140.4 nm, the Trr value is significantly higher than the other three transmittance components, exciting the chirality of mode I, corresponding to the CD peak at 1140.4 nm in Fig. 4(b) with a value of 0.863. Additionally, the Tll spectrum exhibits a sharp asymmetric line shape, indicating the simultaneous excitation of Fano resonance based on BICs at this point.

The structural asymmetry giving rise to BICs serves as a prevalent approach for inducing Fano resonance. Fano resonance, characterized by an asymmetric line shape in scattering, emerges from the intricate interplay between resonant transmission and resonant reflection [39]. In our structure, a distinct Fano profile curve is observed. Qualitative analysis of the transmission spectrum can be conducted using the Fano equation, expressed by the following fitting formula:

$$T_{Fano} = \left| a_1 + i a_2 + \frac{b}{\omega - \omega_0 + ir} \right|^2 \quad (4)$$

Where a_1, a_2, and b are real constants, γ is the total damping loss, and ω_0 is the resonant frequency [40]. $A = a_1 + i a_2$ represents the continuum state, and $B = b/(\omega - {}_i\gamma)$ denotes the discrete state. The Q factor can be expressed as:

$$Q_{rad} = \frac{\omega_0}{2\gamma} \quad (5)$$

Through linear fitting of the Fano profile, we calculated a Q-factor of 1517.5 at $\lambda = 1140.4$ nm. The parameters such as the Q-factor, resonant wavelength, and linewidth can be modulated by adjusting the asymmetry parameter $\Delta S/S$. Here, ΔS represents the area of the detached section on the left annular cylinder, and S denotes the total area of the Si metasurfaces. The relationship between the asymmetry parameter and Q-factor under quasi-BICs resonance is given by the following equation:

$$Q_{rad} = \frac{A}{2k_0} |p_0|^{-2} \left(\frac{\Delta S}{S} \right)^{-2} \quad (6)$$

Where A represents the surface area of the meta-molecule, k_0 is the wave vector of the incident plane wave, and p_0 is the electric dipole moment of the lower half of the nanocube. This indicates that the radiation Q-factor of quasi-BICs is inversely proportional to the square of the asymmetry, given by:

$$Q_{rad} \propto \left(\frac{\Delta S}{S} \right)^{-2} \quad (7)$$

In Fig. 5, we performed a fitting of the relationship between the Q-factor and the asymmetry parameter in a logarithmic coordinate system. The results conform to an inverse square ratio. As the asymmetry parameter increases, the Q-factor decreases. This is attributed to the breaking of symmetry, constructing a radiative channel with free space. With greater asymmetry, the radiative channel widens, implying more energy loss due to radiation, leading to a smaller Q-factor.

To further understand the physical mechanism behind the formation of resonant modes, we utilize Cartesian multipole decomposition to quantitatively identify the multilevel characteristics of eigenmodes. The multipole moments include electric dipole moment (ED), magnetic dipole moment (MD), toroidal dipole moment (TD), electric quadrupole moment (EQ), and magnetic quadrupole moment (MQ), defined as follows:

ED :
$$\boldsymbol{p} = \frac{1}{i\omega} \int \boldsymbol{j} d^3 r \quad (8)$$

MD :
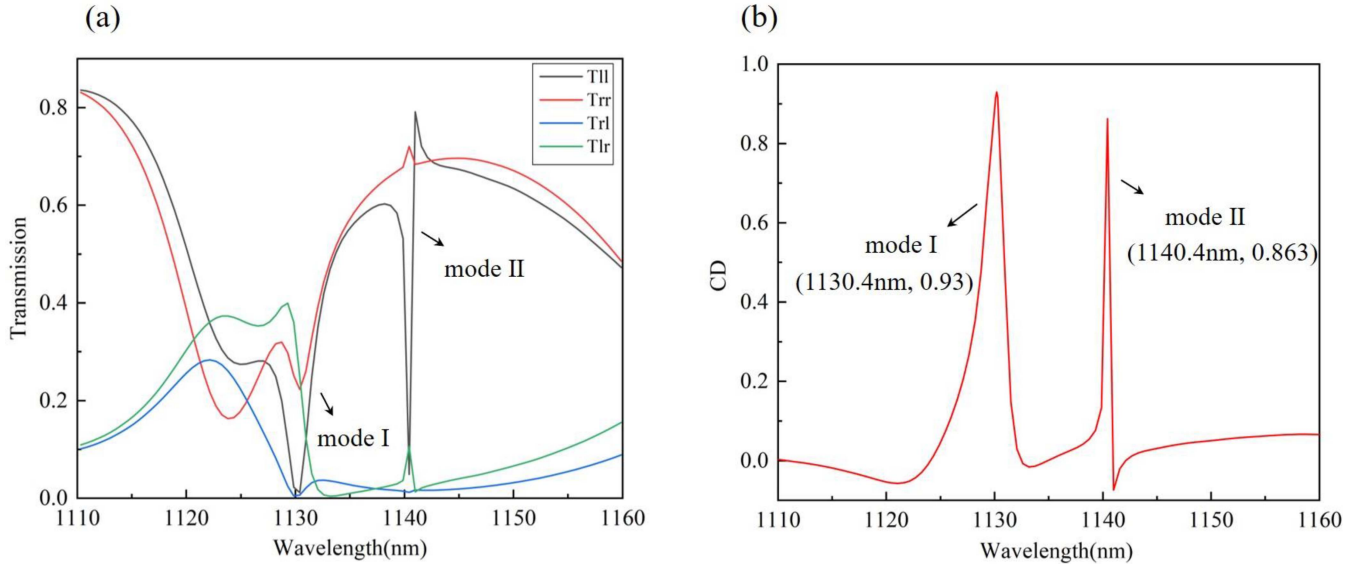$$\boldsymbol{m} = \frac{1}{2c} \int (\boldsymbol{r} \times \boldsymbol{j}) d^3 r \quad (9)$$

Fig. 4. (a) Circularly polarized transmittance components spectrum for the asymmetric structure when $\delta = 30°$. (b) Corresponding CD values.
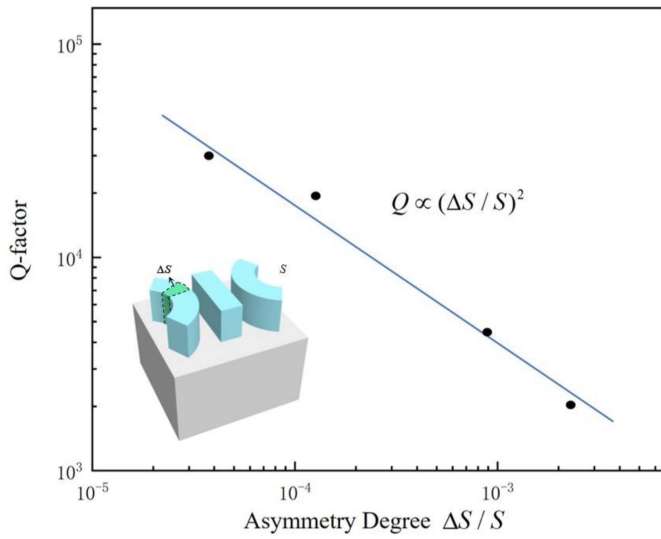

Fig. 5. The relationship between the Q-factor and the asymmetry degree at $\lambda = 1140.4$ nm. The embedded image denotes the definition of the asymmetry degree.

TD :
$$\boldsymbol{T} = \frac{1}{10c} \int [(\boldsymbol{r} \cdot \boldsymbol{j})\boldsymbol{r} - 2r^2\boldsymbol{j}]d^3r. \tag{10}$$

EQ :
$$\boldsymbol{Q}_{\alpha\beta}^{(e)} = \frac{1}{i2\omega} \int [r_\alpha j_\beta + r_\beta j_\alpha - \frac{2}{3}(\boldsymbol{r} \cdot \boldsymbol{j})\delta_{\alpha,\beta}]d^3r. \tag{11}$$

MQ :
$$\boldsymbol{Q}_{\alpha\beta}^{(m)} = \frac{1}{3c} \int [(\boldsymbol{r} \times \boldsymbol{j})\boldsymbol{r}_\beta - (\boldsymbol{r} \times \boldsymbol{j})_\beta \boldsymbol{r}_\alpha]d^3r. \tag{12}$$

Here, c represents the speed of light in vacuum, ω is the angular frequency, $\boldsymbol{r}$ stands for the spatial position vector, and $\boldsymbol{j}$ is the current density.

By extracting electric field, magnetic field and refractive index information through FDTD, and plugging them into the formulas, we calculate the radiated energy for each multipole and the corresponding electromagnetic field distribution at the resonant wavelength, as depicted in Fig. 6:

From the Cartesian multipole decomposition results in Fig. 6(a) and (b), it can be observed that the optical effects at mode I are mainly dominated by MD, corresponding to the counterclockwise circulating current loop in the x-y plane as shown in Fig. 6(c), validating that the resonant mode wavelength at this point is the MD along the negative z-direction. Whereas, mode II is mainly dominated by both MD and TD, corresponding to two oppositely directed circulating current loops in the x-y plane as depicted in Fig. 6(d).

To investigate the impact of structural parameters on the chiroptical effects of the metasurface, we systematically varied the structural period P, thickness t, as well as the length a and width b of the central nanorod, studying their influence on the CD peak positions and magnitudes. All other parameters were maintained consistent with the configuration depicted in Fig. 1. The simulation results are presented in Fig. 7. Fig. 7(a) illustrates that when the P increases from 800 nm to 840 nm, both mode I and mode II undergo a pronounced redshift, accompanied by a slight reduction in CD peak magnitude. Notably, the linewidth of the metasurface remains largely unchanged. Similarly, when the thickness increases from 210 nm to 230 nm, both mode I and mode II experience a redshift. However, unlike the period effect, the CD peak values of both modes increase first and then decrease with the increasing thickness. Fig. 7(c) and (d) show that varying the length of the nanorod from 380 nm to 420 nm has almost no effect on both modes. When the width of the central nanorod increases from 90 nm to 110 nm, both mode I and mode II exhibit a slight redshift, with no significant changes in linewidth and peak magnitude. Therefore, the study indicates that the initial geometric parameters of P = 800 nm, t = 220 nm, a = 400 nm, and b = 100 nm provide excellent performance, facilitating further research and application in
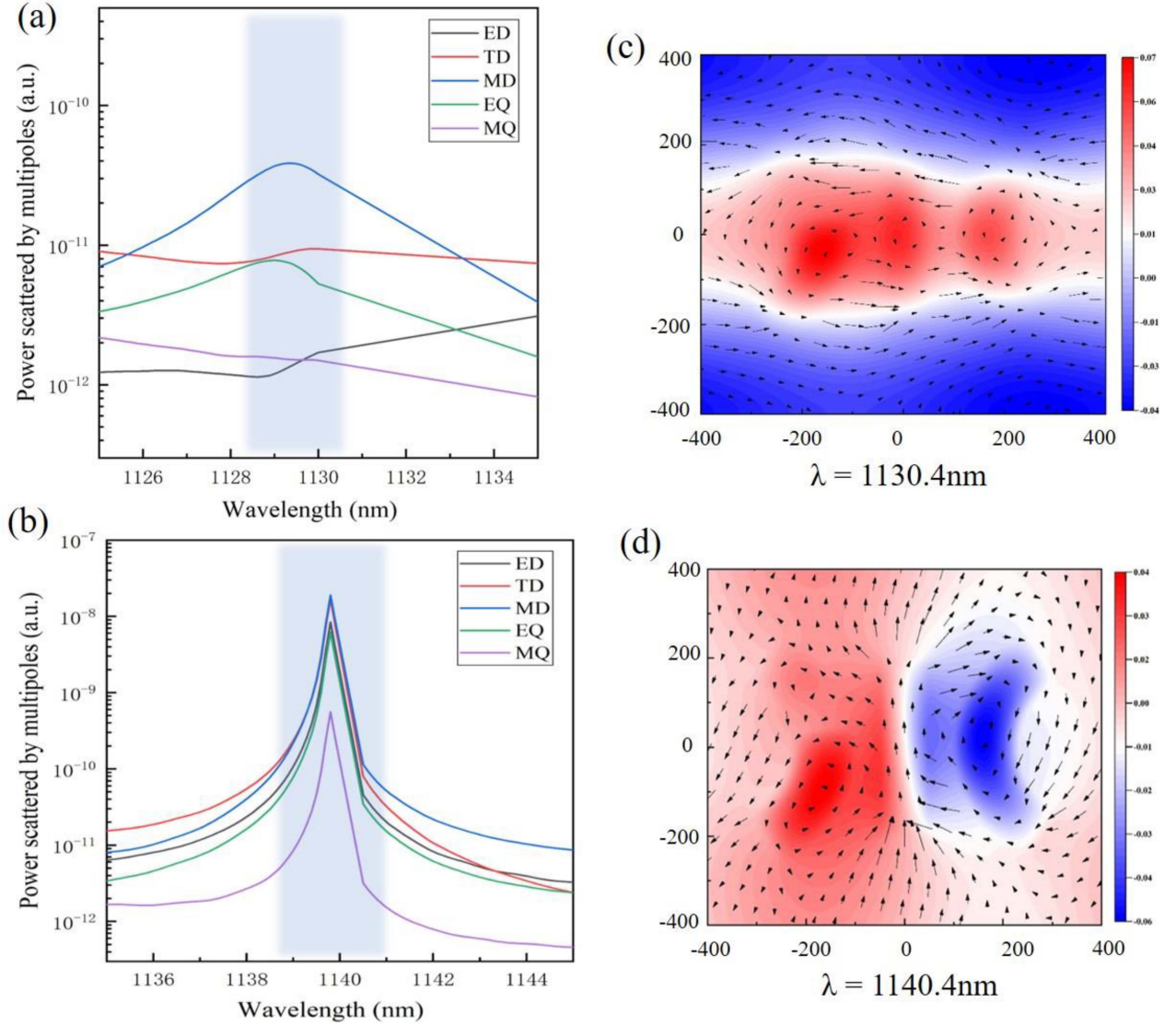
Fig. 6. When $\delta = 30°$, (a) scattered power of various multipole moments for mode I in logarithmic coordinates. (b) Scattered power of various multipole moments for mode II in logarithmic coordinates. (c) Electric field and magnetic field distribution in the x-y plane at $\lambda = 1130.4$ nm for mode I. (d) Electric field and magnetic field distribution in the x-y plane at $\lambda = 1140.4$ nm for mode II. Black arrows represent the displacement current distribution.

sensing. Additionally, by adjusting the P and t, this metasurface can achieve tunable peak shifts to meet the wavelength range requirements in different application scenarios.

Finally, to explore the application of the chiral structure in refractive index sensing, we analyzed the impact of different refractive indices (n) in the surrounding medium on the CD spectrum. Fig. 8(a) illustrates a significant redshift in the CD spectra of mode I and mode II as the gap between structures and the refractive index of the surrounding medium range from 1.00 to 1.08. To further quantitatively assess the refractive index sensing performance, we calculated their sensitivity and FOM. Sensitivity and FOM are critical parameters for measuring refractive index sensing performance and can be defined by the following formulas:

$$S = \frac{\Delta\lambda(nm)}{\Delta n(RIU)} \tag{13}$$

$$FOM = \frac{S(nm/RIU)}{FWHM} \tag{14}$$

where $\Delta\lambda$ represents the shift in wavelength, Δn is the change in refractive index, and FWHM is the full width at half maximum of the CD peak.

In Fig. 8(a), with the change of refractive indices, the CD spectra of curves vary Fig. 8(b) depicts the sensitivity fitting results for the CD spectra of the two modes with varying refractive index. The chiral metasurface designed in this study achieves maximum sensitivity and FOM values of 270.6 nm/RIU and 587.5 RIU^{-1}, respectively. Additionally, in Fig. 8(a), it is observed that the designed structure's CD value reaches 0.979 under a background refractive index of 1.06.

To verify the impact of symmetry breaking-induced BICs and chiral-optical effects on the sensing performance of the structure, we analyzed the wavelength shifts of the resonant transmission
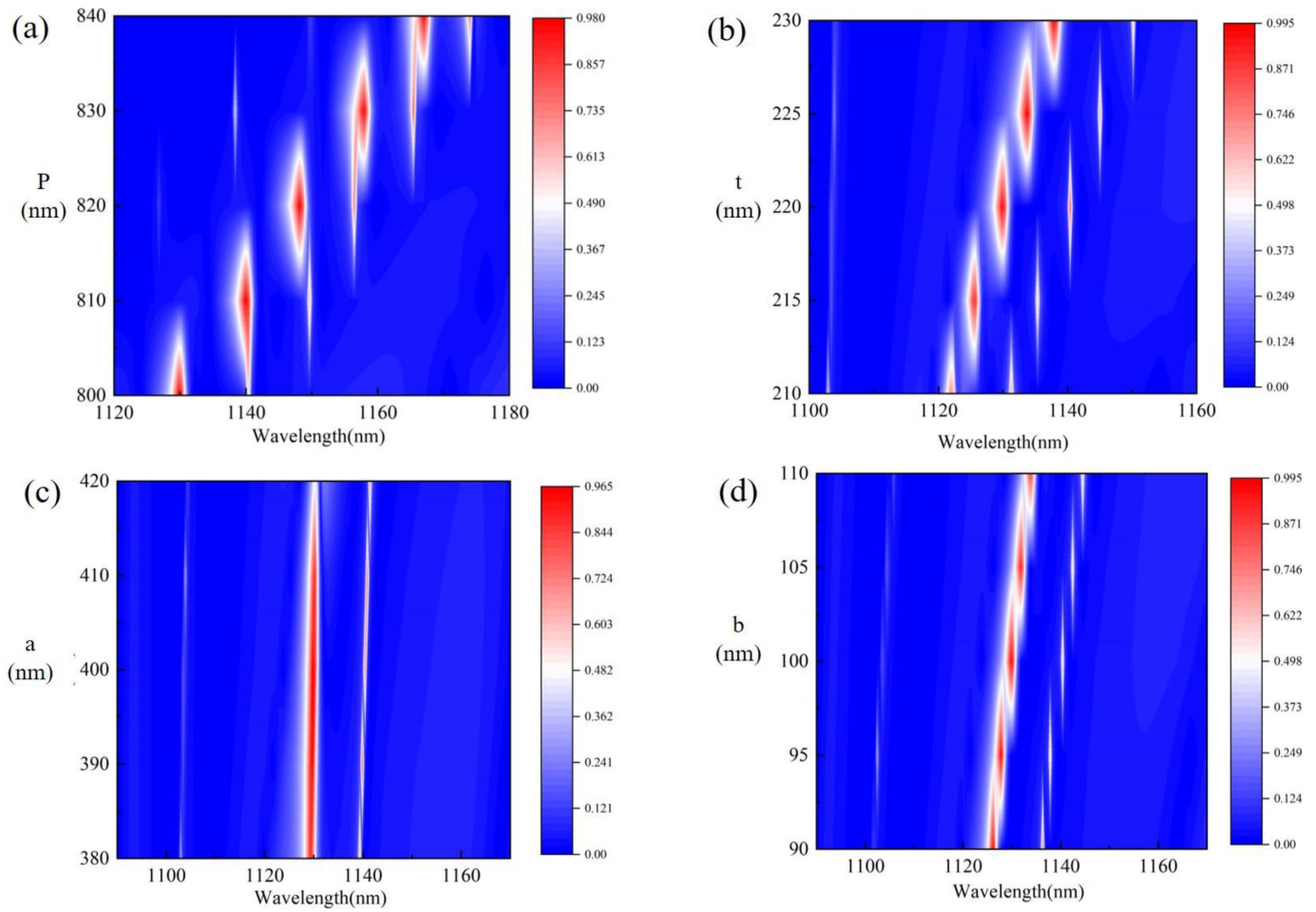
Fig. 7. Color map of CD under different simulation parameters. (a) The period P ranges from 800 nm to 840 nm. (b) The thickness t of the silicon structure ranges from 210 nm to 230 nm. (c) The length a of the intermediate nanorods ranges from 380 nm to 420 nm. (d) The width b of the nanorods ranges from 90 nm to 110 nm.
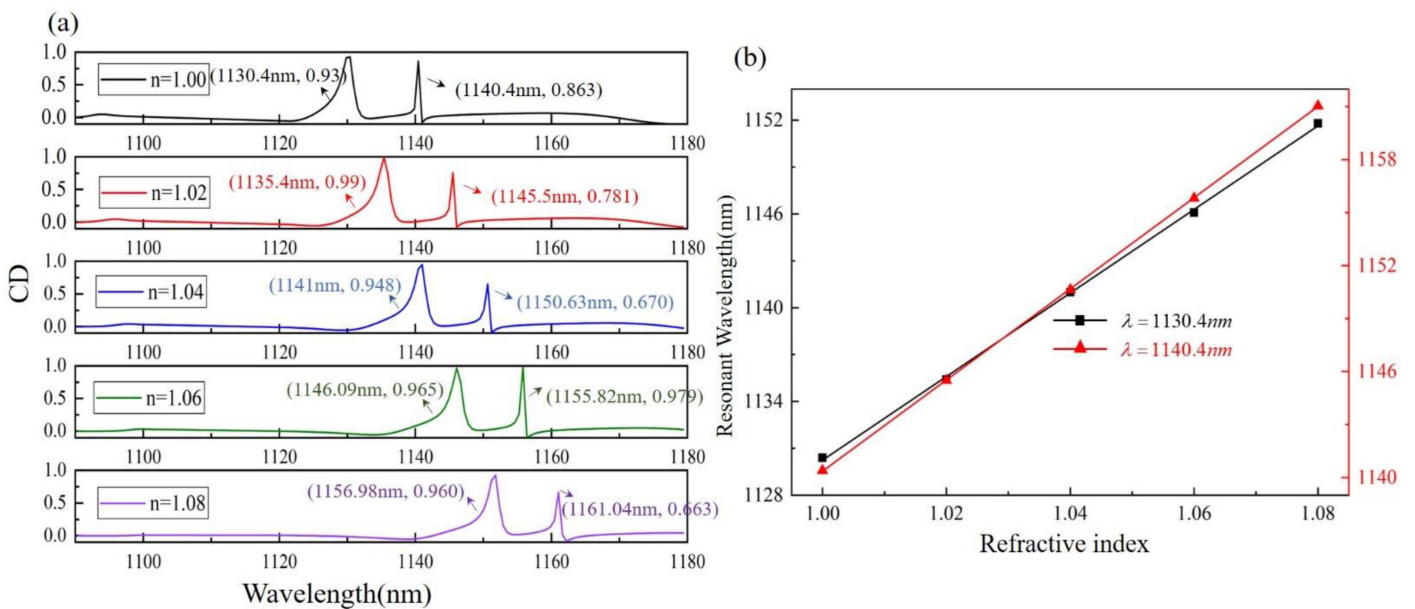

Fig. 8 (a) CD spectra of the two modes with different refractive indices. (b) Resonant wavelength shift of the modes relative to refractive index.
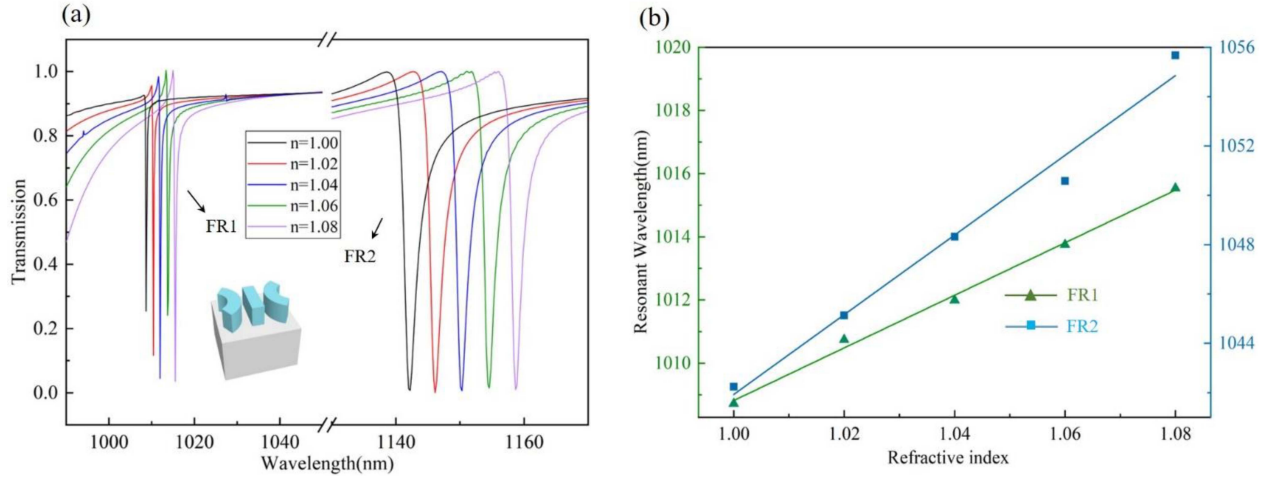
Fig. 9.   (a) Resonance spectra for symmetric structures under different environmental refractive indices. (b) Corresponding resonant wavelength shift of FR1 and FR2 at RI from 1.00 to 1.08.

TABLE I
SENSITIVITY (S) AND THE FIGURE OF MERIT (FOM) IN DIFFERENT MODES

Structures	The symmetric structure		The chiral structure	
Resonant	FR1	FR2	mode I	mode II
Sensitivity (nm/RIU)	96.25	263.9	270.6	265.3
FOM (RIU^{-1})	192.5	94.3	347.2	587.5

spectra under symmetric conditions with varying background refractive indices. In this situation, due to the complete symmetry of the structure, chiral BIC is not excited. Fig. 9(a) depicts the excitation of two Fano resonances, FR1 and FR2, in symmetric structures, with resonance peaks undergoing a redshift as the environmental refractive index increases from 1.00 to 1.08. Fig. 9(b) provides a clearer illustration of the resonance peak shifts. The fitted results reveal sensitivities of 96.25 nm/RIU and 263.9 nm/RIU for FR1 and FR2, respectively, with corresponding FOM values of 192.5 and 94.3. The comparative results are summarized in Table I. It can be observed that, compared to the resonances in the symmetric structure, the sensing performance of the two chiral modes excited in the asymmetric structure is significantly enhanced, confirming the optimization of sensing performance by chiral BICs.

square ratio, the asymmetry is introduced to verify the implementation of quasi-BIC. Multipole moments decomposition and electromagnetic field analysis elucidate that the dominant modes responsible for the chiral response are the MD and TD modes. Tunability of resonance peak positions is achieved through the adjustment of structural parameters, such as period and thickness. Based on CD, we achieve a sensing sensitivity of 270.6 nm/RIU and a FOM of 587.5. We conduct a comparative analysis of the sensing performance of resonant peaks excited under non-chiral conditions, confirming the enhancement of sensing capabilities based on chiral BIC. Our study advances the application exploration of chirality in the sensing field, offering ideas for subsequent research in the development of ultra-broad detection and dynamic sensing of sensors.

IV. CONCLUSION

In summary, our proposed chiral metasurface structure excites dual-band chiral effects based on BIC at 1130.4 nm and 1140.4 nm under symmetry breaking. Through the substantial transmission of one circularly polarized light and the almost complete reflection of another circularly polarized light, the structure has achieved nearly lossless maximum chirality. This results in strong CD with a value of 0.93 and a high Q-factor of 1517.5. In addition, a CD peak value of 0.979 is attained at a background refractive index of 1.06. According to the inverse

REFERENCES

[1] W. J. Choi et al., "Terahertz circular dichroism spectroscopy of biomaterials enabled by kirigami polarization modulators," *Nature Mater.*, vol. 18, no. 8, pp. 820–826, 2019.
[2] N. Yu et al., "Light propagation with phase discontinuities: Generalized laws of reflection and refraction," *Science*, vol. 334, no. 6054, pp. 333–337, 2011.
[3] D. Wang et al., "Efficient generation of complex vectorial optical fields with metasurfacess," *Light: Sci. Appl.*, vol. 10, no. 1, 2021, Art. no. 67.
[4] G. H. Wagnière, *On Chirality and the Universal Asymmetry: Reflections On Image and Mirror Image*. Hoboken, NJ, USA: Wiley, 2007, pp. 3–4.
[5] H. Yang et al., "High efficiency dual-wavelength achromatic metalens via cascaded dielectric metasurfaces," *Opt. Mater. Exp.*, vol. 8, no. 7, pp. 1940–1950, 2018.

[6] S. Wang et al., "Metasurface-based solid poincaré sphere polarizer," *Phys. Rev. Lett.*, vol. 130, no. 12, 2023, Art. no. 123801.

[7] A. O. Govorov et al., "Theory of circular dichroism of nanomaterials comprising chiral molecules and nanocrystals: Plasmon enhancement, dipole interactions, and dielectric effects," *Nano Lett.*, vol. 10, no. 4, pp. 1374–1382, 2010.

[8] Z. Gao, P. Wang, S. Yu, Z. Xu, and T. Zhao, "High circular dichroism optical chiral metasurfaces based on bound states in the continuum," *Symmetry*, vol. 15, no. 7, 2023, Art. no. 1444.

[9] Z. Ma et al., "All-dielectric planar chiral metasurface with gradient geometric phase," *Opt. Exp.*, vol. 26, no. 5, pp. 6067–6078, 2018.

[10] Y. Shi, S. Yu, H. Li, J. Xing, and T. Zhao, "Ultra-high quality factor resonances in a pinwheel-shaped all-dielectric metasurfaces based on bound states in the continuum," *IEEE Photon. J.*, vol. 15, no. 2, Apr. 2023, Art. no. 4600507.

[11] H. Lee et al., "Chiral exceptional point and coherent suppression of backscattering in silicon microring with low loss Mie scatterer," *eLight*, vol. 3, no. 1, 2023, Art. no. 20.

[12] C. W. Hsu, B. Zhen, A. D. Stone, J. D. Joannopoulos, and M. Soljačíc, "Bound states in the continuum," *Nature Rev. Mater.*, vol. 1, no. 19, 2016, Art. no. 16048.

[13] D. C. Marinica, A. G. Borisov, and S. V. Shabanov, "Bound states in the continuum in photonics," *Phys. Rev. Lett.*, vol. 100, 2008, Art. no. 183902.

[14] M. Zhang and X. Zhang, "Ultrasensitive optical absorption in graphene based on bound states in the continuum," *Sci. Rep.*, vol. 5, 2015, Art. no. 8266.

[15] D. N. Maksimov, V. S. Gerasimov, S. Romano, and S. P. Polyutov, "Refractive index sensing with optical bound states in the continuum," *Opt. Exp.*, vol. 28, pp. 38907–38916, 2020.

[16] J. Kuha, "AIC and BICS: Comparisons of assumptions and performance," *Sociol. Methods Res.*, vol. 33, no. 2, pp. 188–229, 2004.

[17] K. P. Burnham and D. R. Anderson, "Multimodel inference: Understanding AIC and BICS in model selection," *Sociol. Methods Res.*, vol. 33, no. 2, pp. 261–304, 2004.

[18] É. Lebarbier and T. Mary-Huard, "Une introduction au critère BICS: Fondements théoriques et interprétation," *J. de la Société Française de Statistique*, vol. 147, no. 1, pp. 39–57, 2006.

[19] P. S. Eis et al., "Accumulation of miR-155 and BICS RNA in human B cell lymphomas," *Proc. Nat. Acad. Sci.*, vol. 102, no. 10, pp. 3627–3632, 2005.

[20] S. Yang et al., "Nanoparticle trapping in a quasi-BICS system," *Amer. Chem. Soc. Photon.*, vol. 8, no. 7, pp. 1961–1971, 2021.

[21] J. Garcia-Guirado et al., "Enhanced chiral sensing with dielectric nanoresonators," *Nano Lett.*, vol. 20, no. 1, pp. 585–591, 2019.

[22] M. Alizadeh and B. R. M. Reinhard, "Plasmonically enhanced chiral optical fields and forces in achiral split ring resonators," *Amer. Chem. Soc. Photon.*, vol. 2, no. 3, pp. 361–368, 2015.

[23] L. Kang et al., "Nonlinear chiral meta-mirrors: Enabling technology for ultrafast switching of light polarization," *Nano Lett.*, vol. 20, no. 3, pp. 2047–2055, 2020.

[24] M. Gandolfi, A. Tognazzi, D. Rocco, C. De Angelis, and L Carletti., "Near-unity third-harmonic circular dichroism driven by a quasibound state in the continuum in asymmetric silicon metasurfacess," *Phys. Rev. A.*, vol. 104, no. 2, 2021, Art. no. 023524.

[25] A. Overvig, N. Yu, and A. Alù, "Chiral quasi-bound states in the continuum," *Phys. Rev. Lett.*, vol. 126, no. 7, 2021, Art. no. 073001.

[26] M. V. Gorkunov, A. A. Antonov, and Y. S. Kivshar, "Metasurfacess with maximum chirality empowered by bound states in the continuum," *Phys. Rev. Lett.*, vol. 125, no. 9, 2020, Art. no. 093903.

[27] T. Shi et al., "Planar chiral metasurfaces with maximal and tunable chiroptical response driven by bound states in the continuum," *Nature Commun.*, vol. 13, 2022, Art. no. 4111, doi: 10.1038/s41467-022-31877-1.

[28] S. H. Oh and H. Altug, "Performance metrics and enabling technologies for nanoplasmonic biosensors," *Nature Commun.*, vol. 9, no. 1, 2018, Art. no. 5263.

[29] A. A. Yanik et al., "Seeing protein monolayers with naked eye through plasmonic Fano resonances," *Proc. Nat. Acad. Sci.*, vol. 108, no. 29, pp. 11784–11789, 2011.

[30] N. Li et al., "DNA-assembled bimetallic plasmonic nanosensors," *Light: Sci. Appl.*, vol. 3, no. 12, 2014, Art. no. e226.

[31] D. Urbonas et al., "Air and dielectric bands photonic crystal microringresonator for refractive index sensing," *Opt. Lett.*, vol. 41, no. 15, pp. 3655–3658, 2016.

[32] H. Lu et al., "Improving the sensitivity of compound waveguide grating biosensor via modulated wavevector," *Appl. Phys. Exp.*, vol. 11, no. 8, 2018, Art. no. 082202.

[33] J. Peng et al., "All-dielectric terahertz metasurfaces with giant extrinsic chirality for dual-mode sensing," *Physica Status Solidi (B)*, vol. 259, no. 10, 2022, Art. no. 2200114.

[34] E. D. Palik, Ed., *Handbook of Optical Constants of Solids*, vol. 3. New York, NY, USA: Academic, 1998.

[35] H. Li et al., "Performance analysis and optimization of high Q-factor toroidal resonance refractive index sensor based on all-dielectric metasurfaces," *Opt. Laser Technol.*, vol. 157, 2023, Art. no. 108752.

[36] Y. Huang et al., "Dual-functional metasurface toward giant linear and circular dichroism," *Adv. Opt. Mater.*, vol. 8, no. 11, 2020, Art. no. 1902061.

[37] Z. F. Sadrieva et al., "Transition from optical bound states in the continuum to leaky resonances: Role of substrate and roughness," *Amer. Chem. Soc. Photon.*, vol. 4, no. 4, 2017, pp. 723–727.

[38] K. Koshelev et al., "Asymmetric metasurfacess with high-Q resonances governed by bound states in the continuum," *Phys. Rev. Lett.*, vol. 121, no. 19, 2018, Art. no. 193903.

[39] A. E. Miroshnichenko, S. Flach, and Y. S. Kivshar, "Fano resonances in nanoscale structures," *Rev. Modern Phys.*, vol. 82, no. 3, 2010, Art. no. 2257.

[40] Y. Yang, I. I. Kravchenko, D. P. Briggs, and J. Valentine, "All-dielectric metasurfaces analogue of electromagnetically induced transparency," *Nature Commun.*, vol. 5, 2014, Art. no. 5753.